



# Spectral Magnetic Helicity of Solar Active Regions between 2006 and 2017

Sanjay Gosain<sup>1</sup> and Axel Brandenburg<sup>2,3,4,5</sup>

<sup>1</sup> National Solar Observatory, 3665 Discovery Drive, Boulder, CO 80303, USA; [sgosain@nso.edu](mailto:sgosain@nso.edu)

<sup>2</sup> Nordita, KTH Royal Institute of Technology and Stockholm University, Roslagstullsbacken 23, SE-10691 Stockholm, Sweden

<sup>3</sup> Department of Astronomy, AlbaNova University Center, Stockholm University, SE-10691 Stockholm, Sweden

<sup>4</sup> JILA and Laboratory for Atmospheric and Space Physics, University of Colorado, Boulder, CO 80303, USA

<sup>5</sup> McWilliams Center for Cosmology & Department of Physics, Carnegie Mellon University, Pittsburgh, PA 15213, USA

Received 2019 March 25; revised 2019 July 4; accepted 2019 July 11; published 2019 September 4

## Abstract

We compute magnetic helicity and energy spectra from about 2485 patches of about 100 Mm side length on the solar surface using data from *Hinode* during 2006–2017. An extensive database is assembled where we list the magnetic energy and helicity, large- and small-scale magnetic helicity, mean current helicity density, fractional magnetic helicity, and correlation length along with the *Hinode* map identification number (MapID), as well as the Carrington latitude and longitude for each MapID. While there are departures from the hemispheric sign rule for magnetic and current helicities, the weak trend reported here is in agreement with the previous results. This is argued to be a physical effect associated with the dominance of individual active regions that contribute more strongly in the better-resolved *Hinode* maps. In comparison with earlier work, the typical correlation length is found to be 6–8 Mm, while the length scale relating the magnetic and current helicities to each other is around 1.4 Mm.

**Key words:** dynamo – magnetohydrodynamics (MHD) – Sun: magnetic fields – turbulence

## 1. Introduction

The Sun’s global magnetic field is produced by a large-scale (LS) dynamo where the overall rotation and vertical density stratification are believed to play important roles in driving what Parker (1955) called cyclonic convection. This means that the flow has a swirl, which can be quantified by its kinetic helicity. Although the details of the solar dynamo are still being debated, there is no doubt that also the Sun’s magnetic field possesses helicity. This was first found by Seehafer (1990), who determined the swirl of electric current lines, i.e., the current helicity, as the product of the vertical components of the magnetic field and current density. Its value was found to be predominantly negative in the northern hemisphere and positive in the southern.

Subsequent work by Pevtsov et al. (1995) confirmed the overall hemispheric dependence but also showed significant scatter. The work of Bao & Zhang (1998) using the Huairou Solar Observing Station of the Beijing Astronomical Observatory also showed scatter, but it was less than what was found by Pevtsov et al. (1995).

The study of solar magnetic helicity received wide-spread attention with the Chapman Conference in Boulder, Colorado during 1998 July 28–31 (Brown et al. 1999). Nowadays, the most commonly employed methods for quantifying magnetic swirl or twist in the Sun include the determination of the mean current helicity, the  $\alpha_{\text{eff}}$  parameter in the force-free field extrapolation, and the gauge-invariant magnetic helicity (Berger & Field 1984; Finn & Antonsen 1985) of the reconstructed force-free magnetic field in the volume above an active region. More recently, there has been growing interest in measuring magnetic helicity spectra for selected patches at the solar surface (Zhang et al. 2014, 2016). The integral of these spectra over all wavenumbers gives the mean magnetic helicity density in the Coulomb gauge. Furthermore, the integrated magnetic helicity spectrum weighted with a  $k^2$  factor gives the mean current helicity density based on the vertical components of the current density and magnetic field in

that patch. Unlike the magnetic helicity, it is gauge-independent but is also expected to be more sensitive to noise resulting from the  $k^2$  factor, which amplifies the contributions from high wavenumbers,  $k$ . Since small-scale (SS) contributions are usually less accurate, the current helicity is expected to be more noisy than the magnetic helicity.

Thus, an important advantage of the spectral approach is that it allows us to filter out certain wavenumber contributions. This is the approach adopted in the present paper. Another advantage of the spectral approach is that it allows us to determine the fractional helicity, which is a non-dimensional measure of the relative amount of magnetic helicity that can give us a sense of the reliability or importance of a particular measurement. For example, one might want to discard all measurements for which the fractional helicity is less than a certain percentage of the maximum possible value.

Finally, we can determine the typical correlation length of the magnetic field, which corresponds to the integral over the spectrum weighted by  $k^{-1}$  and normalized by the mean magnetic energy density. Again, it can be used as a threshold if we are only interested in large active regions, for example.

In a few selected cases, the measurement of magnetic helicity spectra has revealed systematic sign changes separately for LSs and SSs. An example is NOAA 11515, which emerged in the southern hemisphere, but was found to violate the hemispheric sign rule (Lim et al. 2016). The spectral analysis showed that this sign rule violation occurred at LSs, while the SS magnetic helicity still obeyed the hemispheric sign rule. Such magnetic fields with opposite signs at LSs and SSs are called bihelical (Yousef & Brandenburg 2003).

The bihelical nature of magnetic fields is an interesting aspect that is actually expected based on dynamo theory (Seehafer 1996; Ji 1999; Blackman & Brandenburg 2003). Scale-dependent sign changes of the magnetic helicity have also been found in the solar wind (Brandenburg et al. 2011) and at the solar surface (Singh et al. 2018).

Here we provide an extensive study of many of the publicly available magnetograms of *Hinode*, which have a pixel resolution of about 220 km on the Sun. *Hinode*'s resolution is much better than that of the Helioseismic and Magnetic Imager (HMI) on the *Solar Dynamics Observatory*, even though the pixel size in megameters is not so different. One must keep in mind, however, that *Hinode* is not a survey instrument and that observations exist only for selected patches on the Sun.

In an associated online catalog<sup>6</sup> we provide the mean magnetic energy, the mean magnetic helicity, its LS and SS contributions, the current helicity, the fractional helicity, and the correlation length for each of the *Hinode* map identification numbers for about 2485 maps.

## 2. Method

Following the approach of Zhang et al. (2014, 2016) and Zhang & Brandenburg (2018), we compute the magnetic helicity spectrum as

$$H_M(k) = \frac{1}{2} \sum_{k_- < |k| \leq k_+} (\tilde{A}_z \tilde{B}_z^* + \tilde{A}_z^* \tilde{B}_z), \quad (1)$$

where  $\tilde{B}_i(\mathbf{k}, t) = \int B_i(\mathbf{x}, t) e^{i\mathbf{k} \cdot \mathbf{x}} d^2\mathbf{x}$  is the Fourier transform of the three magnetic field components  $i = x, y$  and,  $z$  of a two-dimensional Cartesian patch on the Sun with  $\mathbf{x} = (x, y)$  denoting the position vector,  $\mathbf{k} = (k_x, k_y)$  is the wavevector in the spectral plane,  $k_\pm = k \pm \delta k/2$  are the wavenumbers of an interval of width  $\delta k = 2\pi/L$  around the argument  $k$  of  $H_M(k)$  in Equation (1) in the plane with the area  $L^2$ , with  $L$  being the size of the magnetogram and

$$\tilde{A}_z = (-ik_x \tilde{B}_y + ik_y \tilde{B}_x)/k^2 \quad (2)$$

is the vertical component of the Fourier-transformed magnetic vector potential.

We define the total magnetic energy spectrum in the plane as

$$E_M(k) = \frac{1}{2} \sum_{k_- < |k| \leq k_+} |\tilde{B}_x(\mathbf{k})|^2 + |\tilde{B}_y(\mathbf{k})|^2 + |\tilde{B}_z(\mathbf{k})|^2. \quad (3)$$

As in Zhang et al. (2014), it will be interesting to compare with the contributions from the horizontal and vertical fields,  $E_M^{(h)}$  and  $E_M^{(v)}$ , respectively, which were defined such that, if the two were equal to each other, then both would be an approximation to the total energy, i.e.,  $E_M(k) \approx E_M^{(h)} \approx E_M^{(v)}$ , which requires that we define the individual contributions such that

$$E_M^{(h)} + E_M^{(v)} = 2E_M(k). \quad (4)$$

Specifically, we thus define them as

$$E_M^{(h)}(k) = \sum_{k_- < |k| \leq k_+} |\tilde{B}_x(\mathbf{k})|^2 + |\tilde{B}_y(\mathbf{k})|^2, \quad (5)$$

$$E_M^{(v)}(k) = \sum_{k_- < |k| \leq k_+} |\tilde{B}_z(\mathbf{k})|^2, \quad (6)$$

i.e., without the 1/2 factor in Equation (3), so that Equation (4) is obeyed.

With our approach, we obtain the mean magnetic energy and helicity densities in the plane as

$$\mathcal{E}_M = \int_0^\infty E_M(k) dk, \quad \mathcal{H}_M = \int_0^\infty H_M(k) dk. \quad (7)$$

Since most of the magnetic energy and helicity in the plane comes from the active region and not the space around it, it makes sense to multiply  $\mathcal{E}_M$  and  $\mathcal{H}_M$  by the size of the patch,  $L^2$ . Furthermore, to facilitate comparison with results in the literature, Zhang et al. (2014) chose to compute the energy and helicity over an arbitrarily defined volume of a height of  $L_z = 100$  Mm above the active region. We adopt here the same approach and thus quote the values of

$$e_M = \mathcal{E}_M L^2 L_z \quad \text{and} \quad h_M = \mathcal{H}_M L^2 L_z. \quad (8)$$

We also determine the LS and SS contributions to the magnetic helicity by defining

$$\mathcal{H}_M^{\text{LS}} = \int_0^{k_{\text{LS}}} H_M(k) dk \quad \mathcal{H}_M^{\text{SS}} = \int_{k_{\text{SS}}}^\infty H_M(k) dk, \quad (9)$$

where we chose  $k_{\text{LS}} = 0.4 \text{ Mm}^{-1}$  and  $k_{\text{SS}} = 3 \text{ Mm}^{-1}$  as the limiting wavenumbers marking the end of the LS range and the beginning of the SS range, respectively. This choice can be motivated by inspecting several examples of spectra that show similar signs of spectral magnetic helicity in the ranges  $k < k_{\text{LS}}$  and  $k > k_{\text{SS}}$ ; see the aforementioned website for the online catalog (see footnote 6).

As alluded to above, we also compute the correlation length of the magnetic field, which is defined as

$$\ell_M = \int_0^\infty k^{-1} E_M(k) dk / \int_0^\infty E_M(k) dk. \quad (10)$$

This allows us to compute the fractional helicity as

$$r_M = \mathcal{H}_M / 2\ell_M \mathcal{E}_M. \quad (11)$$

The value of  $r_M$  lies in the range  $-1 \leq r_M \leq 1$ .

## 3. Observational Data

We use high-resolution and high-sensitivity vector magnetograms provided as level-2 data products by the Milne-Eddington gRid Linear Inversion Network (MERLIN) pipeline at the Community Spectropolarimetric Analysis Center of the High Altitude Observatory of the National Center for Atmospheric Research (HAO/CSAC) (doi:10.5065/D6JH3J8D). These vector magnetograms are deduced from the spectropolarimetric scans of solar magnetic regions by the *Hinode* Solar Optical Telescope/Spectro-Polarimeter (SOT/SP) instrument (Tsuneta et al. 2008) that has a diffraction limited field of view of up to  $328'' \times 164''$  and an angular resolution of  $0''.3$ . More details about the *Hinode* SOT/SP instrument and the calibration of data can be found in Lites & Ichimoto (2013) and Lites et al. (2013). The level-2 data products consist of area scans of a variety of target regions, such as active regions, the quiet Sun, polar regions, and repeated small region scans for time evolution studies. For our study, we down-selected these data to include only active regions and pores. The majority (73%) of the selected data are sunspots or active regions with fully formed penumbrae, while the rest (27%) are pores without penumbrae. The level-2 vector magnetograms were resolved for the  $180^\circ$  azimuth ambiguity using the method described in Rudenko & Anfinogentov (2014).

<sup>6</sup> doi:10.5281/zenodo.3338302

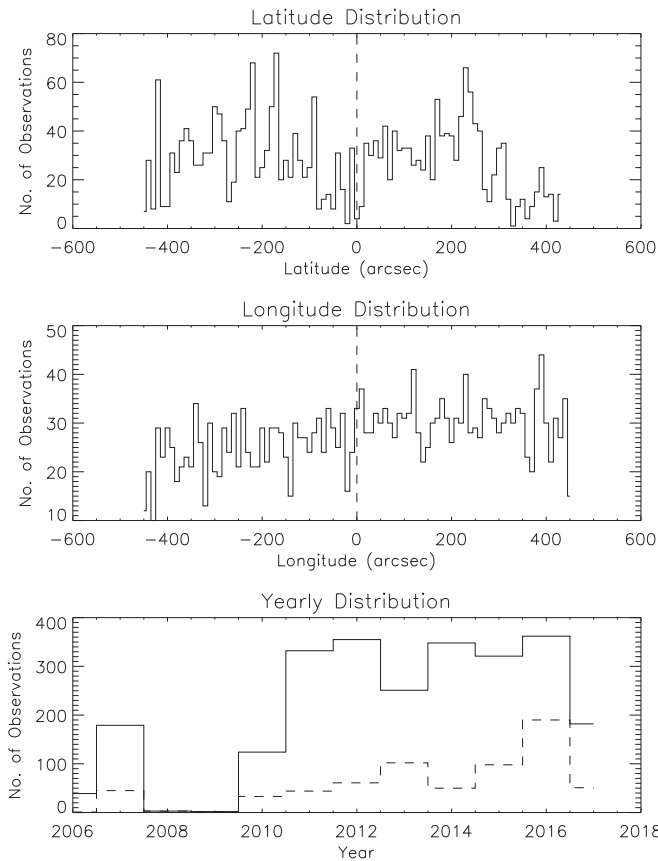


**Figure 1.** Distribution of *Hinode* observations selected for this study in the latitude, longitude, and year-wise shown in the top, middle, and bottom panels, respectively. The solid line in the histogram in the bottom panel represents all observations selected for an analysis, while the dashed line shows the fraction of those containing pores.

We selected the data based on the following criteria:

1. The observed region should be inside the heliocentric angle range of  $0^\circ$  to  $30^\circ$ . This is done to avoid perspective effects and the need to do a heliographic coordinate transformation of the vector magnetograms.
2. The field of view of the observed region should be at least  $96''$  in either direction. This is done to avoid partial/incomplete scans of active regions.
3. The total area occupied by dark umbra or pores in the observed region should be greater than  $(10'')^2$ , or 900 pixels. This is done to avoid selecting very small-sized pores. The umbral area is computed from the continuum intensity map by first removing the limb darkening function and then normalizing the intensity to median value in non-magnetic pixels. Pixels with normalized intensity less than or equal to 0.55 are treated as the umbra or pore.
4. The data that satisfies the above criteria sometimes include undesired characteristics, such as repeated small area scans for time evolution studies of sunspots or active region scans with missing scan lines, bad columns, or partial scans. Thus, as a final criterion, the data is displayed and manually rejected if these undesired characteristics are present.

The distribution of the latitude, longitude, and the year of the selected observations is shown in Figure 1. The yearly

distribution is found to be relatively uniform, except for the time of solar minimum during 2008 and 2009.

*Hinode* observes the target regions with either the normal mode ( $0.''16/\text{pixel}$  sampling) or the fast mode ( $0.''32/\text{pixel}$  sampling). In our selected data set, both modes exist. We convert normal mode scans in our data set to  $0.''32/\text{pixel}$ , so that all maps have the same spatial sampling. Further, in our calculations, we always use  $512 \times 512$  pixels in the region of interest (ROI). If the original data is larger, we extract  $512 \times 512$  ROI centered pixels around the active region or pore. On the other hand, if the original data is smaller, we embed the observed region in the center of a  $512 \times 512$  array with zero padding in adjacent missing pixels.

Finally, we create a database of helicity parameters for each scan, which is uniquely identified by the *Hinode* MapID; see the aforementioned website (see footnote 6), which also contains spectra for each map.

## 4. Results

We processed 2485 vector magnetograms over the solar disk for the years 2006 through 2017, covering in some cases the entire evolution of an active region as it passes the solar disk. Of these magnetograms, 680 correspond to pores (dark regions without penumbrae) and 1805 correspond to fully developed sunspots and active regions with fully developed penumbrae. There can be significant temporal variations of the helicity, which are sometimes associated with the development of flares and coronal mass ejections.

### 4.1. Time–Latitude Distribution of Helicity

*Hinode* data selected here span almost a solar cycle, so we first look at the distribution of the helicity sign and magnitude with time and latitude during the end of cycle 23 and most of cycle 24. In Figure 2, the distributions of  $H_M$ ,  $H_C$ , and  $r_M$  are given. The negative (positive) sign of these parameters are represented in blue (red). As is found in many previous studies, the statistical trend of the negative (positive) sign in the northern (southern) hemisphere is present. The relative amplitude of these parameters is represented by the radius of the circle symbol in Figure 2. We summarize the hemispheric statistics of these parameters in Table 1 with 95% confidence intervals. Hemispheric bias is seen to be present and is significant in  $h_M$ ,  $h_M^{LS}$ , and  $r_M$  in both hemispheres. Although the current helicity ( $H_C$ ) the bias is weak in the north, it is found to be strong in the south.

For SSs,  $h_M^{SS}$  shows a peculiar result in that the sign is predominantly positive in both north (75%) and south (83%). This is perhaps because, as seen in Table 2, most of the helicity is accounted for by the LS component. Typically, for all of the data, the amplitude of the SS helicity is about  $10^4$  times smaller than the LS helicity. Thus, most of the contribution must come from the LS part. There is good agreement between the  $h_M$ ,  $h_M^{LS}$ , and  $r_M$  statistics.

### 4.2. Latitudinal Dependence

The dependence of the fractional magnetic helicity on Carrington latitude  $\lambda$  is shown in Figure 3. This relation is extremely noisy, although there is still a clear negative correlation with  $\lambda$ . Specifically, we find

$$r_M(\lambda) = -0.004 - 0.17 \sin \lambda. \quad (12)$$

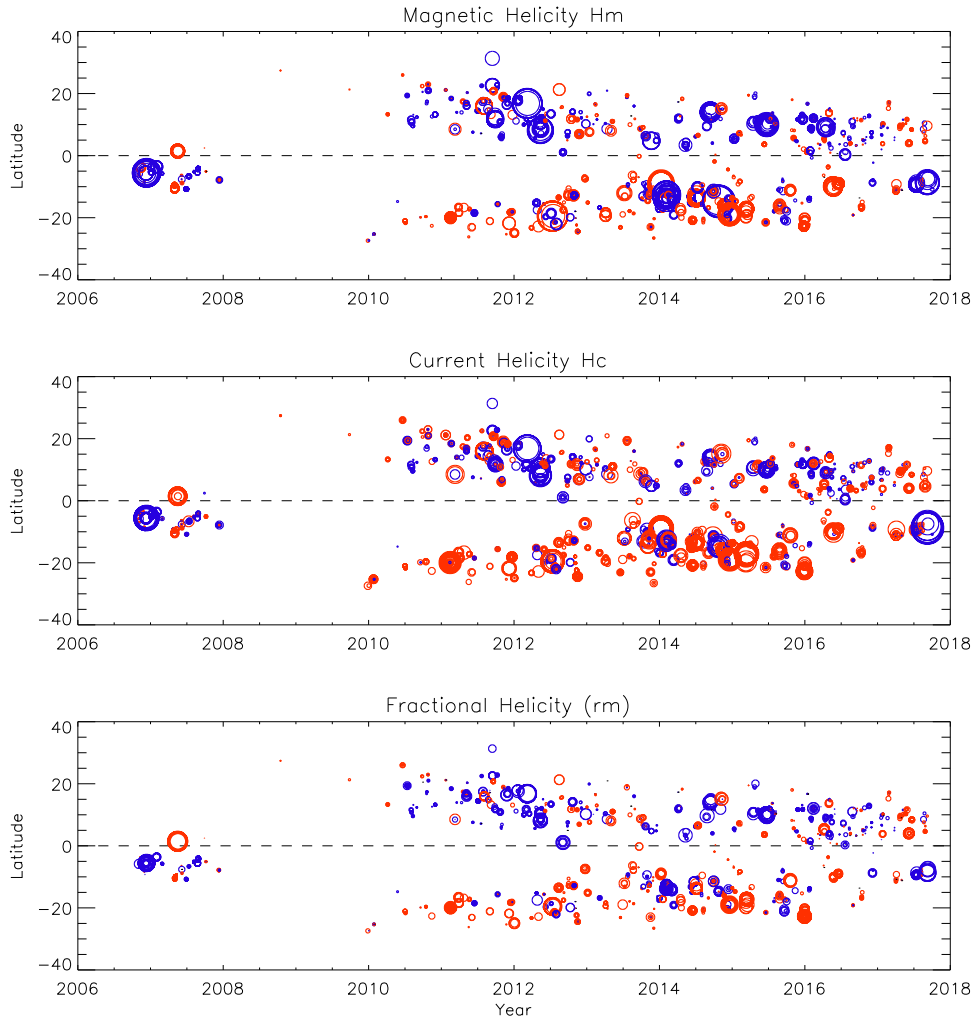


**Figure 2.** Time–latitude distribution of helicity parameters. Top panel shows the distribution of magnetic helicity density ( $\mathcal{H}_M$ ), the middle panel the current helicity density ( $\mathcal{H}_C$ ), and the bottom panel shows the fractional helicity ( $r_M$ ). The blue (red) circles represent negative (positive) sign of these parameters. In the top two panels, we scaled the diameter of the circles to the square root of the normalized amplitudes, since the values vary over a large range. In the bottom panel, the values are fractional quantities between  $\pm 1$ , so the radii of the circles are just scaled to the  $r_M$  value. The biggest circle in each of the three plots corresponds, respectively, to  $37.8 \times 10^{42} \text{ Mx}^2$ ,  $875.2 \times 10^{24} \text{ G}^2 \text{ cm}^{-1}$ , and 0.61.

**Table 1**  
Percent of Active Regions Following Hemispheric Rule

Hemisph.	$h_M[\%]$	$h_M^{\text{LS}}[\%]$	$h_M^{\text{SS}}[\%]$	$\mathcal{H}_C[\%]$	$r_M[\%]$
North	$62 \pm 3$	$61 \pm 3$	$24 \pm 2$	$47 \pm 3$	$62 \pm 3$
South	$59 \pm 3$	$58 \pm 3$	$82 \pm 2$	$73 \pm 2$	$59 \pm 3$

The dependences of  $\mathcal{H}_M(t)$  and  $\mathcal{H}_C(t)$  on the latitude (not shown) are even more noisy, but they also show negative correlations:

$$h_M(\lambda) = -0.56 - 3.2 \sin \lambda \quad [\text{G}^2 \text{ Mm}^4], \quad (13)$$

$$\mathcal{H}_C(\lambda) = 18 - 170 \sin \lambda \quad [\text{G}^2 \text{ km}^{-1}]. \quad (14)$$

Previous statistical studies of the latitudinal variation of helicity parameters derived from other observations also show a similar scatter (Hagino & Sakurai 2004; Xu et al. 2007; Gosain et al. 2013). It is also observed that the hemispheric helicity trend varies during the solar cycle. Hagino & Sakurai (2005) studied the annual variation of the helicity trend and found that the hemispheric sign preference is more likely to be present during the maximum phase than during the minimum

phase of the solar cycle. Bao et al. (2000) found that the hemispheric trend was reversed during the rising phase of solar cycle 23. Later, Zhang et al. (2010) found similar signatures both during the declining phase of cycle 22 and during the rising phase of cycle 23. For the helicity of the nonaxisymmetric SS magnetic field, Pipin et al. (2019) confirmed the usual hemispheric sign rule along with a sign reversal near the end of cycle 24. They also found that the LS axisymmetric magnetic field tends to have the opposite sign to that of the nonaxisymmetric field, except again later in cycle 24, when both have the same sign.

During the activity minimum phase, the statistics are generally poorer due to a small number of active regions than during the maximum phase. Here we only present the latitudinal distribution of all observations during a cycle, which is a better statistic and is less prone to biases due to selection effects, such as the size and number of active regions during a single year. Synoptic full-disk vector magnetograms are generally better suited for the study of the time variation of the hemispheric helicity trend.

The amount of scatter is rather significant and seems to support a similar trend from earlier findings suggesting that at a

**Table 2**  
Summary of Data for NOAA 10930

y	m	d	h:m	$e_M$	$h_M$	$h_M^{LS}$	$h_M^{SS}$	$\mathcal{H}_C$	$r_M$	$\ell_M$	$\lambda$	$\mathcal{L}$	MapID
2006	12	9	10:00	10.8	-8.8	-8.8	-2.3	-202	-0.22	7.56	-5.7	-26.9	30107
2006	12	9	11:20	11.0	-8.7	-8.7	-5.5	-179	-0.21	7.57	-5.7	-26.3	30108
2006	12	9	12:40	11.1	-8.6	-8.5	2.7	-157	-0.20	7.64	-5.7	-25.5	30109
2006	12	9	14:00	11.2	-8.0	-8.0	4.8	-140	-0.19	7.60	-5.7	-24.8	30110
2006	12	9	17:10	11.3	-8.1	-8.1	10.7	-117	-0.19	7.61	-5.7	-23.0	30111
2006	12	9	22:00	11.8	-8.1	-8.0	11.9	-128	-0.18	7.61	-5.7	-20.4	30112
2006	12	10	1:00	12.1	-8.1	-8.0	4.9	-144	-0.17	7.62	-5.7	-18.7	30113
2006	12	10	10:55	13.7	-8.2	-8.2	6.4	-197	-0.16	7.44	-5.7	-12.6	30114
2006	12	10	21:00	14.4	-14.7	-14.5	-4.4	-489	-0.27	7.66	-5.7	-7.6	30115
2006	12	11	3:10	15.2	-20.9	-20.7	-14.7	-720	-0.35	7.73	-5.7	-4.1	30116
2006	12	11	8:00	15.5	-24.3	-24.0	-11.6	-806	-0.40	7.71	-5.7	-1.5	30117
2006	12	11	11:10	15.6	-26.8	-26.6	-12.1	-802	-0.44	7.84	-5.7	0.4	30118
2006	12	11	13:10	15.7	-28.3	-28.0	-10.6	-848	-0.46	7.81	-5.7	1.9	30119
2006	12	11	17:00	16.2	-29.9	-29.7	-6.4	-850	-0.47	7.87	-5.7	3.5	30120
2006	12	11	20:00	16.2	-30.7	-30.4	-10.8	-862	-0.48	7.86	-5.7	5.2	30121
2006	12	11	23:10	16.2	-32.4	-32.2	-12.7	-822	-0.50	7.92	-5.7	7.0	30122
2006	12	12	3:50	16.7	-33.0	-32.8	-16.7	-892	-0.51	7.78	-5.7	9.6	30123
2006	12	12	10:10	16.3	-33.0	-32.8	-19.2	-875	-0.52	7.80	-5.5	13.6	30124
2006	12	12	15:30	15.8	-29.7	-29.5	-17.1	-781	-0.48	7.77	-5.7	16.0	30125
2006	12	12	17:40	15.6	-28.1	-27.9	-17.5	-696	-0.46	7.81	-5.7	17.2	30126
2006	12	12	20:30	15.0	-25.8	-25.7	-11.2	-596	-0.43	7.88	-5.7	18.8	30127
2006	12	13	4:30	14.8	-29.1	-29.0	-14.1	-638	-0.49	7.91	-5.7	23.2	30128
2006	12	13	7:50	14.2	-28.3	-28.2	-8.7	-618	-0.50	7.96	-5.7	25.1	30129

Note.  $e_M$  is in  $10^{32}$  erg,  $h_M$  and  $h_M^{LS}$  are in  $10^{42}$  Mx $^2$ ,  $h_M^{SS}$  is in  $10^{38}$  Mx $^2$ ,  $\mathcal{H}_C$  is in  $10^{24}$  G $^2$  cm $^{-1}$ ,  $r_M$  is dimensionless,  $\ell_M$  is in Mm, and  $\lambda$  and  $\mathcal{L}$  are in degrees.

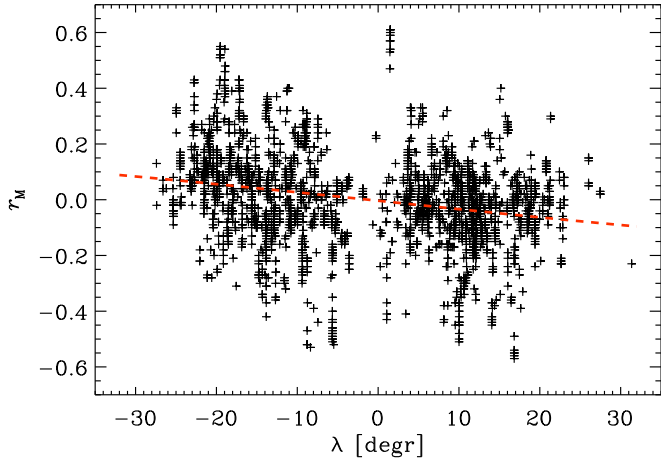


Figure 3. Dependence of the fractional magnetic helicity on the latitude.

higher resolution, the general hemispheric sign rule deteriorates; see the earlier findings by Bao & Zhang (1998) and Pevtsov et al. (1995), where the latter showed much a stronger scatter than the former. Similarly, using low-resolution vector synoptic maps, Gosain et al. (2013) found a weak hemispheric trend with a smaller scatter in the current helicity density.

#### 4.3. Time Dependence

There is a general hemispheric preference with most of the active regions having a negative magnetic helicity in the north and a positive one in the south. However, there can also be significant departures from this hemispheric preference. Figure 4 shows the evolution of  $e_M(t)$ ,  $h_M(t)$ ,  $\ell_M(t)$ , and  $r_M(t)$  for all 2485 maps.

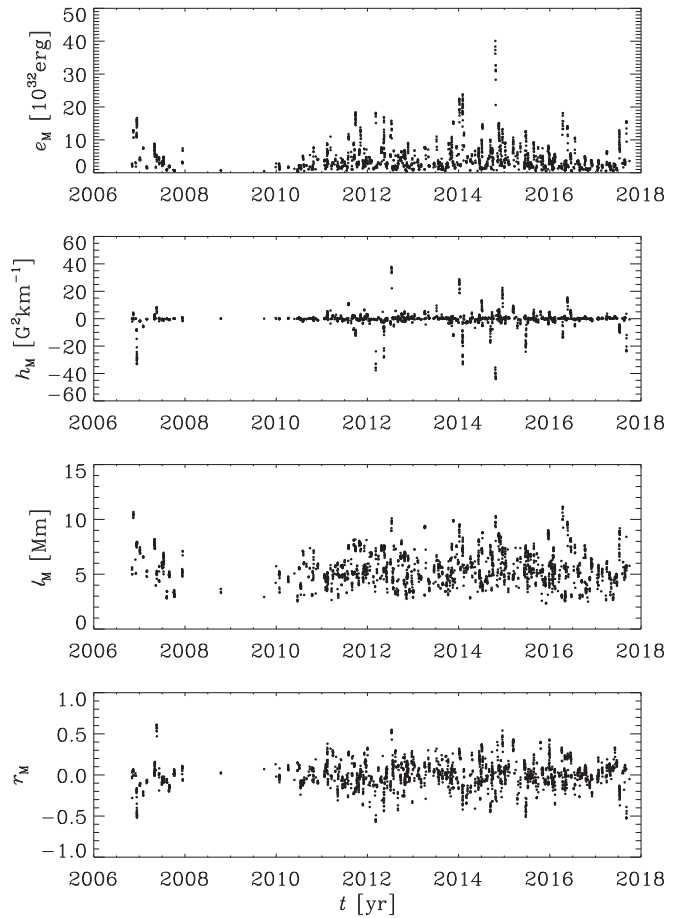
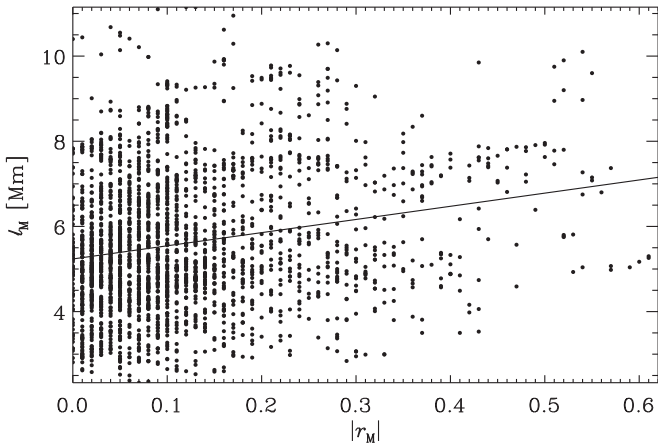


Figure 4. Temporal variation of  $e_M(t)$ ,  $h_M(t)$ ,  $\ell_M(t)$ , and  $r_M(t)$  for all 2485 maps.



**Figure 5.** Scatter plot between  $r_M(t)$  and  $\ell_M(t)$ .

for all 2485 maps, regardless of position or selection effects arising from the fact that particularly interesting active regions have been observed repeatedly. One clearly sees overall enhanced activity during the solar maximum around 2014 and only very few measurements during the solar minimum around 2008 and 2009. While  $e_M(t)$  does show some intense spikes of activity on a timescale of 1–2 yr, the spikes in  $h_M(t)$  are even more extreme. This is reminiscent of earlier findings that used a related method applied to synoptic vector magnetograms (Brandenburg et al. 2017). On the other hand,  $r_M(t)$  now seems to be less spiky than what has been found from the synoptic vector magnetograms. This difference can well be caused by the aforementioned selection effects resulting from the fact that particularly interesting regions have been observed more frequently.

The overall variation of  $\ell_M(t)$  is rather small and the values are around 6 Mm both during the minimum and maximum. Similar values have also been found with both HMI and the Huairou Solar Observing Station (Zhang et al. 2016). This value of  $\ell_M$  is significantly smaller than what has been found using the synoptic vector magnetograms from HMI, where  $\ell_M$  was found to fluctuate around 20 Mm, or from the Synoptic Optical Long-term Investigations of the Sun (SOLIS), where  $\ell_M$  was found to fluctuate around 15 Mm (Singh et al. 2018).

As already emphasized by Singh et al. (2018), the numerical value of  $\ell_M$  must not be interpreted as a physically identifiable length scale. In fact, since it is defined as a weighted inverse wavenumber, it might make sense to identify  $2\pi\ell_M$  with a physically relevant length scale.

The fact that  $\ell_M$  is about three times larger when it is determined from the synoptic maps is interesting and has not previously been noticed. This may indicate that a synoptic magnetogram is different from an actual magnetogram. It could be caused by an anisotropy resulting from the assembly of different magnetograms in the longitudinal direction. This aspect is worth revisiting in future.

Earlier work by Zhang et al. (2016) showed that  $\ell_M(t)$  displays a clear modulation with the solar cycle, where  $\ell_M(t)$  varied between 6 Mm during the solar minimum and 8 Mm during the solar maximum. No such clear variation can be seen from our current data. Nevertheless, looking at a scatter plot between  $r_M(t)$  and  $\ell_M(t)$  does suggest a positive, albeit very noisy, correlation between the two; see Figure 5.

In this connection, it is useful to recall the findings of Yang & Zhang (2012) and Zhang & Yang (2013) that the quiet Sun

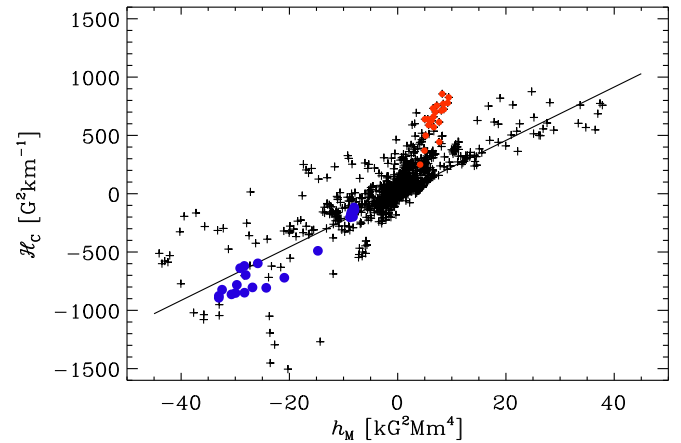


**Figure 6.** Scatter plot showing the dependence of the current helicity on the magnetic helicity. The blue (red) symbols show the data for NOAA 10930 (NOAA 12297) only.

contributes much less to the cyclic variation than active regions. This could explain the relatively small variation of  $\ell_M(t)$  in our data, because with *Hinode*, we expect a stronger and more accurate contribution from the quiet Sun than for the Huairou Solar Observing Station.

#### 4.4. Relation with Current Helicity

In homogeneous turbulence, there is a relation between the magnetic helicity spectrum and the current helicity spectrum such that  $H_C(k) = k^2 H_M(k)$ . There is no such clear relationship between magnetic and current helicity in physical space, although the two might still be related to each other by the square of a length scale.

In Figure 6, we show the dependence of magnetic helicity on current helicity as a scatter plot. We see a positive dependence with a slope of  $23 \times 10^{-6} \text{ Mm}^{-5}$ . Adopting, again, our reference volume of  $V = (100 \text{ Mm})^3$  used in our calculations of  $H_M(k)$ , we find  $k^2 = 23 \text{ Mm}^{-2}$ , i.e.,  $k = 4.8 \text{ Mm}^{-1}$  or  $2\pi/k = 1.3 \text{ Mm}$ . This corresponds to the scale of granulation. Such an association between the typical scale of current helicity patterns and granulation has not previously been possible to make.

Figure 6 seems to show evidence of a separate group of points with a slightly steeper correlation. This group of points comprises solely those belonging to NOAA 12297, as is demonstrated by the red symbols in that figure. This is an active region at  $-17^\circ$  latitude, which has a rather large value of  $r_M$  of 0.3–0.4; see Table 3. However, the more important exception here is that for NOAA 12297,  $h_M$  is rather small ( $5\text{--}9 \text{ kG}^2 \text{ Mm}^4$ ) in comparison with NOAA 10930, where it reaches values of around  $20\text{--}30 \text{ kG}^2 \text{ Mm}^4$ .

#### 4.5. Case Study: NOAA 10930

The tabulated values of various parameters for the well-studied active region NOAA 10930 during 2006 December were already shown in Table 2. An example of helicity and energy spectra for this active region during 2006 December 12 at 20:30 UT is shown in Figure 7. We find that the magnetic helicity for this active region is negative during 2006 December 9–13. This sign is opposite to the expectation from the hemispheric helicity rule. The negative sign is seen in all helicity indicators in Table 2, except for the SS magnetic

**Table 3**  
Summary of Data for NOAA 12297

y	m	d	h:m	$e_M$	$h_M$	$h_M^{LS}$	$h_M^{SS}$	$\mathcal{H}_C$	$r_M$	$\ell_M$	$\lambda$	$\mathcal{L}$	MapID
2015	3	9	20:48	5.9	5.0	4.7	10.1	370	0.36	4.66	-20.0	-21.6	115255
2015	3	10	7:45	6.7	6.2	5.8	18.3	626	0.41	4.49	-19.6	-18.7	115262
2015	3	10	11:04	6.4	5.7	5.3	20.6	588	0.39	4.57	-18.1	-19.1	115264
2015	3	11	3:15	7.3	6.6	6.2	24.5	660	0.39	4.60	-17.1	-28.2	115267
2015	3	11	8:10	7.7	6.7	6.4	17.9	571	0.36	4.74	-17.1	-25.5	115268
2015	3	11	22:01	9.2	8.1	7.8	14.6	712	0.35	4.95	-17.1	-17.8	115271
2015	3	11	22:35	8.7	8.5	8.2	16.3	724	0.40	4.89	-17.1	-17.5	115272
2015	3	12	3:22	9.4	9.4	9.1	23.2	826	0.41	4.85	-17.2	-14.8	115273
2015	3	12	4:43	9.5	9.2	9.0	15.0	778	0.40	4.88	-17.2	-14.1	115274
2015	3	12	10:37	10.7	8.2	7.8	25.9	856	0.31	4.90	-17.2	-10.8	115275
2015	3	12	13:52	9.0	8.4	8.0	23.8	771	0.39	4.78	-17.2	-4.6	115276
2015	3	12	15:50	10.0	7.2	6.9	16.2	756	0.29	4.89	-17.2	-4.6	115277
2015	3	12	21:00	9.5	7.0	6.6	15.1	701	0.30	4.83	-17.2	-5.1	115278
2015	3	12	21:48	7.5	7.7	7.3	14.5	614	0.43	4.74	-17.2	-4.7	115279
2015	3	13	3:01	8.6	6.6	6.2	21.4	732	0.32	4.68	-17.2	-1.8	115280
2015	3	13	10:30	7.5	5.6	5.2	17.0	639	0.32	4.54	-17.2	2.4	115282
2015	3	13	20:00	7.2	5.0	4.6	18.6	639	0.30	4.61	-17.2	5.0	115283
2015	3	14	1:50	6.9	5.2	4.9	11.2	498	0.31	4.78	-17.2	10.8	115285
2015	3	15	9:30	5.9	7.7	7.5	11.1	444	0.43	5.94	-17.3	28.1	115292
2015	3	16	23:00	3.8	4.2	4.1	1.5	250	0.41	5.28	-19.0	24.5	115302

Note.  $e_M$  is in  $10^{32}$  erg,  $h_M$  and  $h_M^{LS}$  are in  $10^{42}$  Mx $^2$ ,  $h_M^{SS}$  is in  $10^{38}$  Mx $^2$ ,  $\mathcal{H}_C$  is in  $10^{24}$  G $^2$  cm $^{-1}$ ,  $r_M$  is dimensionless,  $\ell_M$  is in Mm, and  $\lambda$  and  $\mathcal{L}$  are in degrees.

helicity,  $h_M^{SS}$ , during the early stage of the active region evolution from December 9 12:40 UT to December 10 10:55 UT, after which  $h_M^{SS}$  is negative. It is interesting to note that, during the early stages of flux emergence, this active region has a similar pattern of the magnetic helicity as NOAA 11515 (Lim et al. 2016), i.e., with opposite signs at LSs and SSs.

The active region was flare productive and led to three M-class, three X-class, and several C-class flares. Many authors have reported strong rotating motion in one of the spots in this group (Yan et al. 2009). Using the three-dimensional nonlinear force-free field extrapolation method, Park et al. (2010) computed the relative coronal magnetic helicity for this active region to be about  $-4.3 \times 10^{43}$  Mx $^2$  just before an X3.4 flare on 2006 December 13. In comparison, our magnetic helicity estimate,  $h_M$ , for this time is about  $-2.6 \times 10^{43}$  Mx $^2$ . We notice that the time of the peak helicity in this active region from Park et al. (2010) and our estimates is the same, i.e., around 3:50 to 10:10 UT on 2006 December 12. Park et al. (2010) suggest that the evolution of helical structures of the opposite sign to the active region dominant helicity sign led to flaring activity in this active region.

Ravindra et al. (2011) studied the evolution of net electric currents in this active region and found that the dominant current in the two opposite magnetic polarities is of the opposite sign, i.e., upward electric current in one polarity and downward in another. Further, they found that the net current in both polarities decreases before the flares and attributed this decrease to an increase in the non-dominant oppositely signed currents in each polarity.

The helicity spectra in the top panel of Figure 7 do show helicity of both signs in general, but the dominant sign is negative when averaged over logarithmically spaced wavenumber bins. The evolution of such helicity spectra at different scales and their relationship with flaring and/or eruptive activity could be insightful. We defer such study in flaring regions to a future work.

#### 4.6. Spectral Energy for Vertical and Horizontal Fields

It is instructive to look at magnetic energy spectra separately for horizontal and vertical (or radial) magnetic fields. The two are remarkably similar at all wavenumbers; see Figure 7. This is rather different from the earlier results by Zhang et al. (2014),<sup>7</sup> who found significant departures at SSs, where the horizontal contribution was found to exceed the vertical one by a factor of about three.

The reason for the SS excess of horizontal over vertical field strengths may well be physical, but it is striking that with the higher resolution of *Hinode*, the two spectra track each other much better than with HMI. Looking at Figure 7, the two spectra agree nearly perfectly up to  $k = 10$  Mm $^{-1}$ , which corresponds to a scale of  $(2\pi/10)$  Mm  $\approx 600$  km. This leads us to expect that with an even higher resolution, such as that of Daniel K. Inouye Solar Telescope, we may continue to see the two spectra tracking each other up to larger wavenumbers at higher resolutions. It also suggests that, if we regard the wavenumber where the spectra depart from each other as the resolution limit, this limit is poorer than previously anticipated. Indeed, with HMI, we see departures already at scales of around 2 Mm. Much of this departure is possibly caused by intrinsic artifacts outside the strong-field regions in the HMI magnetograms. Those should be investigated in subsequent analyses.

## 5. Conclusions

The purpose of the present work was to use *Hinode* data to provide a comprehensive survey of spectral magnetic helicity. The data turn out to be of considerably higher quality than those used in earlier analyses of HMI and SOLIS data. This became evident when comparing magnetic energy spectra separately for vertical and horizontal magnetic field

<sup>7</sup> We use here the opportunity to correct a labeling error in their Figure 2, where the energies of vertical and horizontal fields should have been swapped.

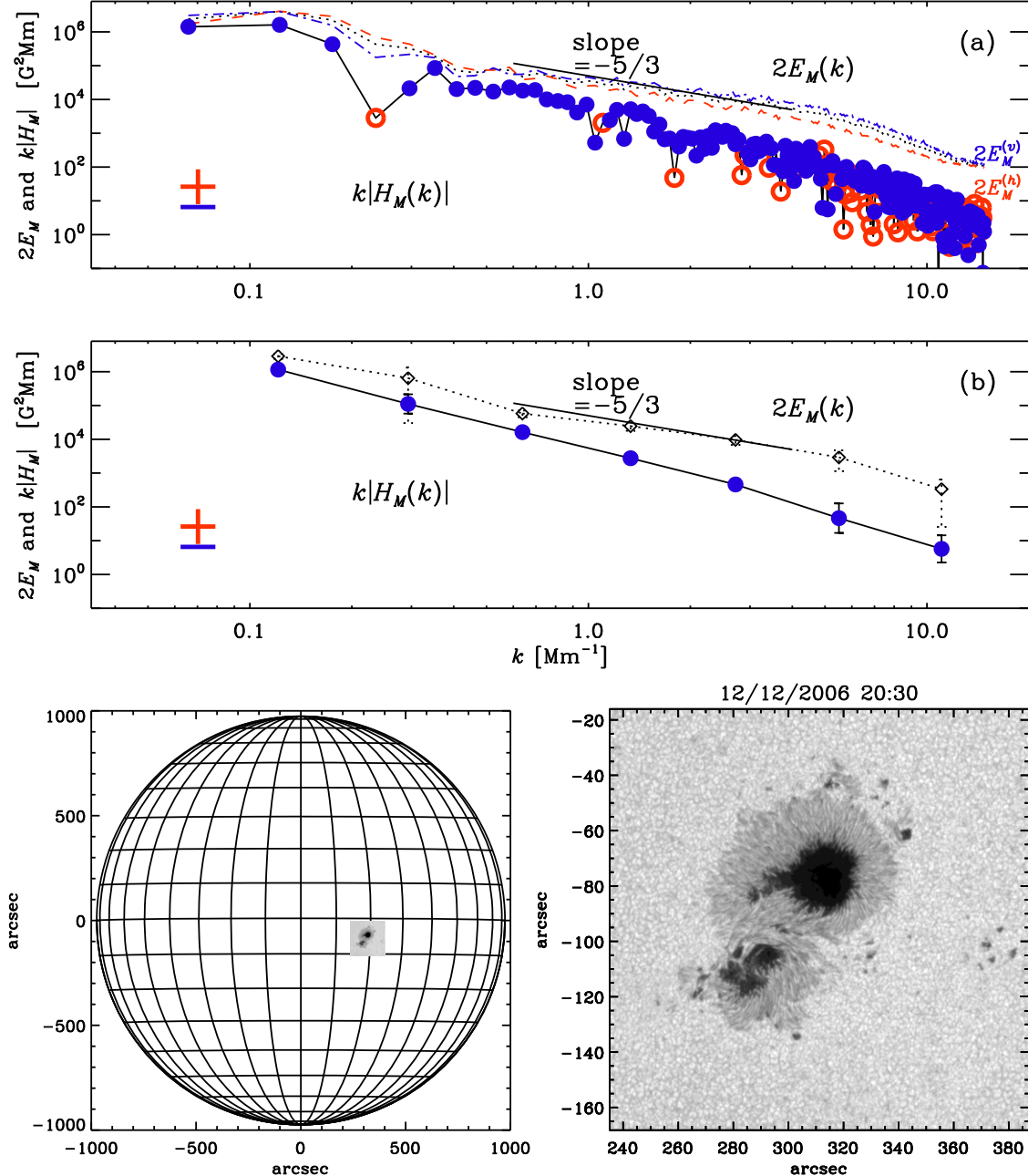


**Figure 7.** (a)  $2E_M(k)$  (dotted line) and  $k|H_M(k)|$  (solid line) for NOAA 10930 at 20:30 UT on 2006 December 12. Positive (negative) values for  $H_M(k)$  are indicated by open (closed) symbols, respectively.  $2E_M^{(h)}(k)$  (red dashed) and  $2E_M^{(v)}(k)$  (blue dotted-dashed) are shown for comparison. (b) Same as (a), but the magnetic helicity is averaged over broad, logarithmically spaced wavenumber bins.

components. Unlike earlier work using HMI, which showed significant departure between the two at  $k = 3 \text{ Mm}^{-1}$  (Zhang et al. 2014), the present analysis shows the two spectra tracking each other up  $k = 10 \text{ Mm}^{-1}$ .

The correlation length,  $\ell_M$ , on the other hand, appears to be rather similar between current and earlier analyses. However, there are differences in comparison with similar results using synoptic magnetograms. Those differences are tentatively associated with the anisotropy resulting from combining magnetograms of different times into a new map.

A major surprise arising from our work is the poor obedience of the hemispheric sign rule of both the magnetic and current helicity. We argued before that the magnetic helicity should be much less affected by noise than the current helicity, but this is

not supported by the current data. The reason for this is not obvious. Looking, for example, at the case of NOAA 10930, we see that the spectrum is not actually very noisy, but that it has the same sign at almost all wavenumbers. Moreover, NOAA 10930 was located in the southern hemisphere, but its magnetic helicity had the same sign as that normally expected for the northern hemisphere. This may then suggest that the hemispheric sign rule violations are not connected with measurement uncertainties, but they may instead be physical. While this is a plausible proposal, it remains curious as to why much weaker fluctuations are generally seen at poorer resolutions. One possibility is that there are significant systematic errors that tend to produce magnetic helicity in agreement with the hemispheric sign rule. Extreme evidence

for this comes from the results of the analysis of synoptic magnetograms (Brandenburg et al. 2017; Singh et al. 2018), where very little departure from the hemispheric sign rule has been found. In some cases, those results with poorer resolutions even showed wavenumber-dependent sign reversals of magnetic helicity that agreed with theoretical expectations (Singh et al. 2018). Such an interpretation in which measurement errors would display a systematic hemispheric dependence would be difficult to accept. It would also raise the question of what is the nature of such systematic errors that produce, or reproduce, the expected sign rule.

Another interpretation of our results could be that the measurements at poorer resolutions are actually real, but that the effect of individual active regions becomes subdominant at poorer resolutions. The high-resolution *Hinode* images, on the other hand, resolve significant details, which makes their contribution dominant. If this is true, we must accept that the magnetic helicity of individual active regions can significantly deviate from the hemispheric sign rule, while the more diffuse background field obeys the potentially scale-dependent hemispheric sign rule rather well. This interpretation is further supported by a recent reanalysis of synoptic vector magnetograms using the parity-even and parity-odd  $E$  and  $B$  mode polarizations (Brandenburg 2019), which avoid the uncertainty associated with the  $\pi$  ambiguity. Those results showed a much clearer sign reversal toward low wavenumbers. This was interpreted to be due to the weak-field contributions that are far from active regions, where the  $\pi$  ambiguity is more problematic in conventional methods.

*Hinode* is a Japanese mission developed and launched by ISAS/JAXA, collaborating with NAOJ as a domestic partner and NASA and STFC (UK) as international partners. Scientific operation of the *Hinode* mission is conducted by the *Hinode* science team organized at ISAS/JAXA. This team mainly consists of scientists from institutes in the partner countries. Support for the post-launch operation is provided by JAXA and NAOJ (Japan), STFC (UK), NASA (USA), ESA, and NSC (Norway). We thank Maarit Käpylä, Alexei Pevtsov, Ilpo Virtanen, and Nobumitsu Yokoi for providing a splendid atmosphere at the Nordita-supported program on Solar Helicities in Theory and Observations. We also thank the anonymous referee for constructive remarks. This work was supported in part through the National Science Foundation, grant AAG-1615100,

and the University of Colorado through its support of the George Ellery Hale visiting faculty appointment.

## ORCID iDs

Sanjay Gosain <https://orcid.org/0000-0002-5504-6773>  
Axel Brandenburg <https://orcid.org/0000-0002-7304-021X>

## References

- Bao, S. D., Ai, G. X., & Zhang, H. Q. 2000, *JApA*, **21**, 303
- Bao, S. D., & Zhang, H. 1998, *ApJL*, **496**, L43
- Berger, M., & Field, G. B. 1984, *JFM*, **147**, 133
- Blackman, E. G., & Brandenburg, A. 2003, *ApJL*, **584**, L99
- Brandenburg, A. 2019, ApJ, submitted (arXiv:1906.03877)
- Brandenburg, A., Petrie, G. J. D., & Singh, N. K. 2017, *ApJ*, **836**, 21
- Brandenburg, A., Subramanian, K., Balogh, A., & Goldstein, M. L. 2011, *ApJ*, **734**, 9
- Brown, M. R., Canfield, R. C., & Pevtsov, A. A. 1999, Magnetic Helicity in Space and Laboratory Plasmas (Washington, DC: AGU)
- Finn, J. M., & Antonsen, T. M. 1985, CoPPC, **9**, 111123
- Gosain, S., Pevtsov, A. A., Rudenko, G. V., & Anfinogentov, S. A. 2013, *ApJ*, **772**, 52
- Hagino, M., & Sakurai, T. 2004, *PASJ*, **56**, 831
- Hagino, M., & Sakurai, T. 2005, *PASJ*, **57**, 481
- Ji, H. 1999, *PhRvL*, **83**, 3198
- Lim, E.-K., Yurchyshyn, V., Park, S.-H., et al. 2016, *ApJ*, **817**, 39
- Lites, B. W., Akin, D. L., Card, G., et al. 2013, *SoPh*, **283**, 579
- Lites, B. W., & Ichimoto, K. 2013, *SoPh*, **283**, 601
- Park, S.-H., Chae, J., Jing, J., Tan, C., & Wang, H. 2010, *ApJ*, **720**, 1102
- Parker, E. N. 1955, *ApJ*, **122**, 293
- Pevtsov, A. A., Canfield, R. C., & Metcalf, T. R. 1995, *ApJL*, **440**, L109
- Pipin, V. V., Pevtsov, A. A., Liu, Y., & Kosovichev, A. G. 2019, *ApJL*, **877**, L36
- Ravindra, B., Venkatakrishnan, P., Tiwari, S. K., & Bhattacharyya, R. 2011, *ApJ*, **740**, 19
- Rudenko, G. V., & Anfinogentov, S. A. 2014, *SoPh*, **289**, 1499
- Seehafer, N. 1990, *SoPh*, **125**, 219
- Seehafer, N. 1996, *PhRvE*, **53**, 1283
- Singh, N. K., Käpylä, M. J., Brandenburg, A., et al. 2018, *ApJ*, **863**, 182
- Tsuneta, S., Ichimoto, K., Katsukawa, Y., et al. 2008, *SoPh*, **249**, 167
- Xu, H., Gao, Y., Zhang, H., et al. 2007, *AdSpR*, **39**, 1715
- Yan, X.-L., Qu, Z.-Q., Xu, C.-L., Xue, Z.-K., & Kong, D.-F. 2009, *RAA*, **9**, 596
- Yang, S., & Zhang, H. 2012, *ApJ*, **758**, 61
- Yousef, T. A., & Brandenburg, A. 2003, *A&A*, **407**, 7
- Zhang, H., & Brandenburg, A. 2018, *ApJL*, **862**, L17
- Zhang, H., Brandenburg, A., & Sokoloff, D. D. 2014, *ApJL*, **784**, L45
- Zhang, H., Brandenburg, A., & Sokoloff, D. D. 2016, *ApJ*, **819**, 146
- Zhang, H., Sakurai, T., Pevtsov, A., et al. 2010, *MNRAS*, **402**, L30
- Zhang, H., & Yang, S. 2013, *ApJ*, **763**, 105